The Astrophysical Journal, 923:276 (17pp), 2021 December 20 https://doi.org/10.3847/1538-4357/ac2f9b

Thomson Scattering in the Lower Corona in the Presence of Sunspots

Pascal Saint-Hilaire[1], Juan Carlos Martínez Oliveros[1], and Hugh S. Hudson[2]
[1] Space Sciences Laboratory, University of California, Berkeley, CA, USA; pascal@ssl.berkeley.edu
[2] School of Physics and Astronomy, University of Glasgow, Glasgow, UK
Received 2021 September 2; revised 2021 October 12; accepted 2021 October 12; published 2021 December 29

Abstract

Polarized scattered light from low (few tens of megameter altitudes) coronal transients has been recently reported in Solar Dynamics Observatory/Helioseismic and Magnetic Image (HMI) observations. In a classic paper, Minnaert (1930) provided an analytic theory of polarization via electron scattering in the corona. His work assumed axisymmetric input from the photosphere with a single-parameter limb-darkening function. This diagnostic has recently been used to estimate the free-electron number and mass of HMI transients near the solar limb, but it applies equally well to any coronal material, at any height. Here we extend his work numerically to incorporate sunspots, which can strongly effect the polarization properties of the scattered light in the low corona. Sunspot effects are explored first for axisymmetric model cases, and then applied to the full description of two sunspot groups as observed by HMI. We find that (1) as previously reported by Minnaert, limb darkening has a strong influence, usually increasing the level of linear polarization tangential to the limb; (2) unsurprisingly, the effects of the sunspot generally increase at the lower scatterer altitudes, and increase the larger the sunspot is and the closer to their center the scatterer subpoint is; (3) assuming the Stokes $Q > 0$ basis to be tangential to the limb, sunspots typically decrease the Stokes Q/I polarization and the perceived electron densities below the spotless case, sometimes dramatically; and (4) typically, a sizeable non-zero Stokes U/I polarization component will appear when a sunspot's influence becomes non-negligible. However, that is not true in rare cases of extreme symmetry (e.g., scattering mass at the center of an axisymmetric sunspot). The tools developed here are generally applicable to an arbitrary image input.

Unified Astronomy Thesaurus concepts: Spectropolarimetry (1973); Solar corona (1483); Solar coronal transients (312)

1. Introduction

Martínez Oliveros et al. (2014), Saint-Hilaire et al. (2014), and J. C. Martinez et al. (2021, in preparation) have reported on the observations by the Solar Dynamics Observatory's (SDO; Pesnell et al. 2012) Helioseismic and Magnetic Imager (HMI; Schou et al. 2012; Scherrer et al. 2012) of above-the-limb emissions from loops/prominence systems and ejected mass above them in two strong flares: SOL2013-05-13T15:48 (GOES class X2.8) and SOL2017-09-10T15:35 (GOES class X8.2).

In particular, Saint-Hilaire et al. (2014) and Martínez Oliveros et al. (2014) make note of a linearly polarized component, which they attribute to Thomson scattering. From this we can infer the number of free electrons. Assuming charge neutrality and an average atomic number, the total mass of the coronal scattering material can also be inferred directly. In these new HMI observations, above the bright loops, the degree of linear polarization appears equal (within the error bars) to the amount theoretically expected in the sunspotless case described by Minnaert (1930). At lower altitude, within the bright flare loops, the amount of polarization is typically less than that predicted by Minnaert (1930). This was attributed to the addition of an unpolarized thermal emission (Jejčič & Heinzel 2009; Saint-Hilaire et al. 2014; Jejčič et al. 2018).

The absence of Stokes U polarization (when Stokes Q is locally defined as being in the tangential ($Q > 0$) or radial ($Q < 0$) directions with respect to center of the Sun) hints at the fact that sunspots have little impact in the two cases mentioned above, as their presence would almost surely break the symmetry and create non-zero Stokes U polarization (this work). Furthermore the amount of Stokes Q/I polarization is either close to the theoretical expectations of Minnaert (1930) with a limb-darkening coefficient of $\upsilon \approx 0.55$ (appropriate for HMI's 6173 Å wavelength of observation) or below it (as stated above, the polarization can be below the expectation from pure Thomson emission when observing the hot bright loop itself).

While focused on the visible portion of the solar spectrum, Minnaert's treatment essentially applies to all wavelengths where material scatters light above an optically thick layer with a sharp transition (and negligible emission above it), a situation that, roughly, occurs from the high end of the microwave spectrum to the UV regime.

In this work, we numerically explore the effects of sunspots and limb intensity profiles on the predicted flux and polarization of scattering material in the corona, adding to Minnaert's spotless (but fully analytical) calculations. In general, our calculations do not deal with continuum wavelengths longer than the millimeter waves or shorter than the near-UV, or with the wings of spectral lines with strong coronal opacity (such as Lyα; Derouich 2018). Following a brief review of the general theory, we will consider the case of a model axisymmetric sunspot, then two actual "real" sunspots.

2. Theory and Geometry

In classical electrodynamics, the oscillating electric field of an electromagnetic radiation incident on a charged particle provokes an oscillation of that particle along the incident field's direction (or polarization vector). The accelerated charge then radiates at the same frequency as the incident wave, with a

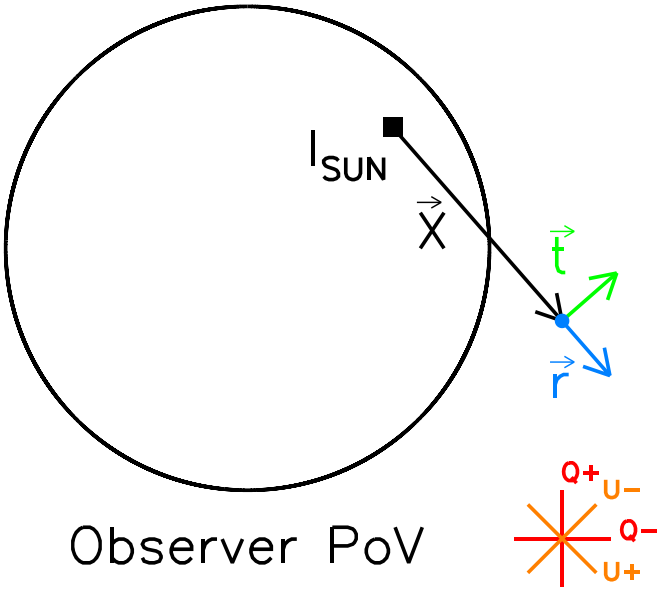

Figure 1. Geometry from the observers's (e.g., at Earth) point of view (PoV), including Stokes Q and U basis.

dipole intensity pattern (radiating more strongly in a direction perpendicular to its oscillatory motion). When the oscillating charged particle is a free electron, and as long as the incoming light's energy is much less than the rest mass of the electron, this process remains elastic and is called Thomson scattering.

The Thomson-scattering differential cross-section is given by Jackson (1975) as

$$\left(\frac{d\sigma}{d\Omega}\right)_T = r_e^2 \ |\boldsymbol{\epsilon}^* \cdot \boldsymbol{\epsilon_0}|^2 \ , \tag{1}$$

where r_e is the classical electron radius (2.82×10^{-15} m), and $\boldsymbol{\epsilon_0}$ and $\boldsymbol{\epsilon}$ are the incoming and outgoing photon polarization vectors (the asterisk denotes complex conjugation). Assuming that the incoming radiation is unpolarized, the volume emissivities (radiated energy per unit time, per unit volume of scattering material, per unit solid angle, and optionally per unit frequency or wavelength) of an infinitesimal scattering element of free-electron density n_e are given by

$$\varepsilon_t = r_e^2 \frac{F}{2} n_e \tag{2}$$

$$\varepsilon_r = r_e^2 \frac{F}{2} n_e \sin^2\chi \tag{3}$$

where F is the unpolarized flux incident on the scattering element (energy radiated per unit time and per unit area; possibly, also per unit frequency or wavelength). χ is the scattering angle (the angle between the incident flux and the flux scattered toward the observer), ε_t is the emissivity of light linearly polarized along $\boldsymbol{t}$, and ε_r is the emissivity of light linearly polarized along $\boldsymbol{r}$, where $\boldsymbol{t}$ is perpendicular to the plane of scattering (a plane containing the source element, the scattering element, and the observer), and $\boldsymbol{r}$ is in the scattering plane, perpendicular to the scatterer–observer line (Figures 1 and 2).

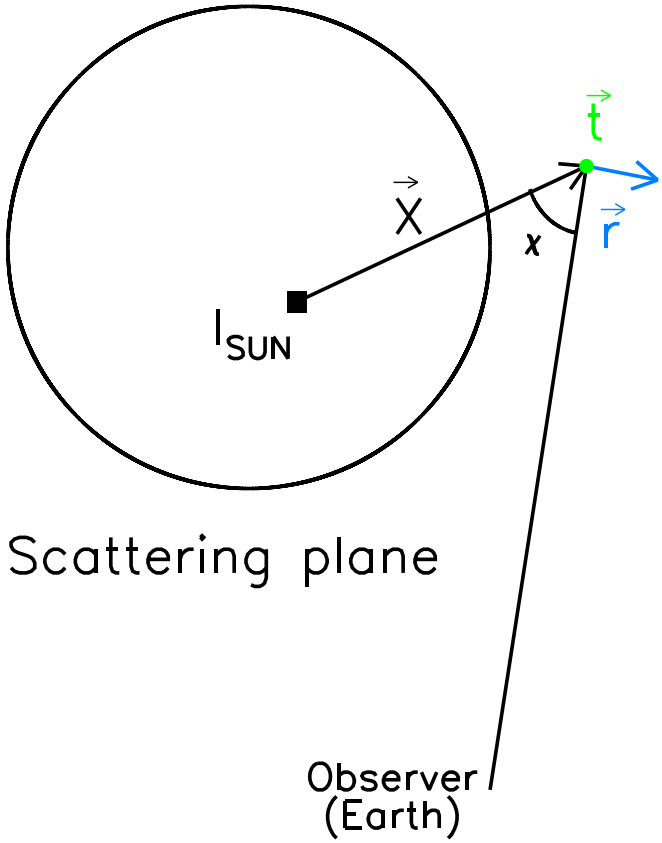

Figure 2. Geometry in the plane of scattering.

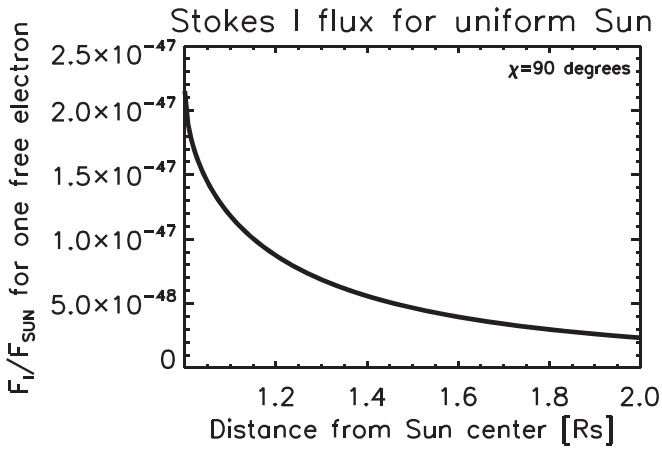

Figure 3. Thomson-scattered Stokes I flux, relative to the solar flux (uniform Sun) and scattering angle $\chi = 90°$.

The differential emissivities per unit solid angle of incoming solar flux are given by

$$\eta_t = \frac{d\varepsilon_t}{d\Omega_{\rm sun}}, \tag{4}$$

$$= \frac{1}{2} r_e^2 \ n_e \ I_{\rm sun}, \tag{5}$$

$$\eta_r = \frac{d\varepsilon_r}{d\Omega_{\rm sun}}, \tag{6}$$

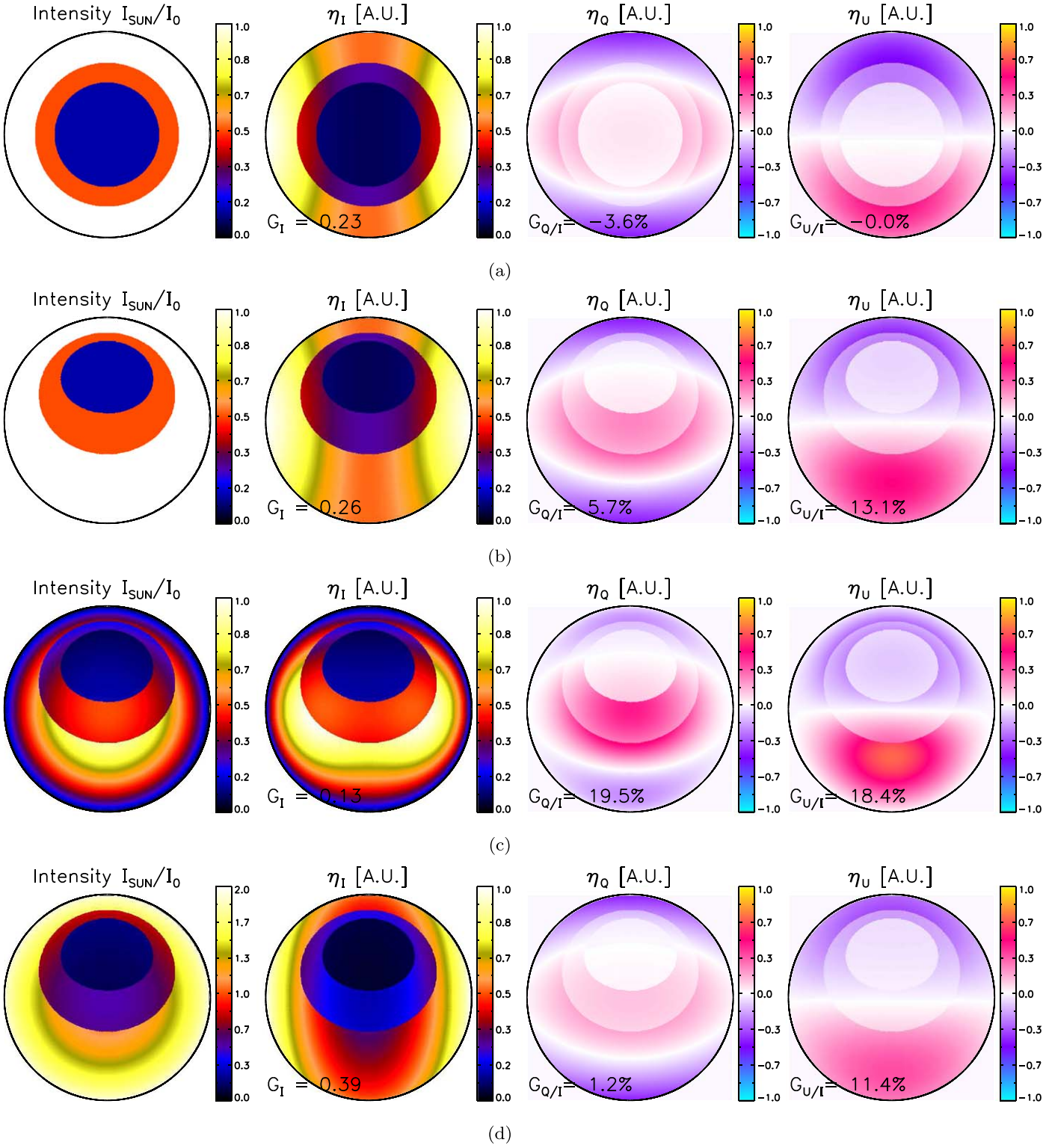

Figure 4. (a) Model sunspot centered on the scatterer solar subpoint: $d = 1.04$, $\upsilon = 0$; (b) model sunspot centered 2° north of the scatterer subpoint: $d = 1.04$, $\upsilon = 0$; (c) model sunspot centered 2° north of the scatterer subpoint: $d = 1.04$, $\upsilon = 1$ (strong limb darkening); and (d) model sunspot centered 2° north of the scatterer subpoint: $d = 1.04$, $\upsilon = -1$ (limb "brightening").

$$= \frac{1}{2} r_e^2 \, n_e \, I_{\rm sun} \sin^2 \chi. \quad (7)$$

The Stokes I, Q, U, and V parameters are often used to fully characterize incoming light of *any* wavelength. They are phaseless power observables typically expressed in fluxes (energy per time and per unit area, sometimes also per unit frequency or wavelength). We shall hence express our results in those quantities. There are no doubt more compact mathematical forms, but our approach offers useful intermediary diagnostics. Thomson scattering from unpolarized sources does not produce circularly polarized flux, and Stokes V shall henceforth be omitted throughout this paper.

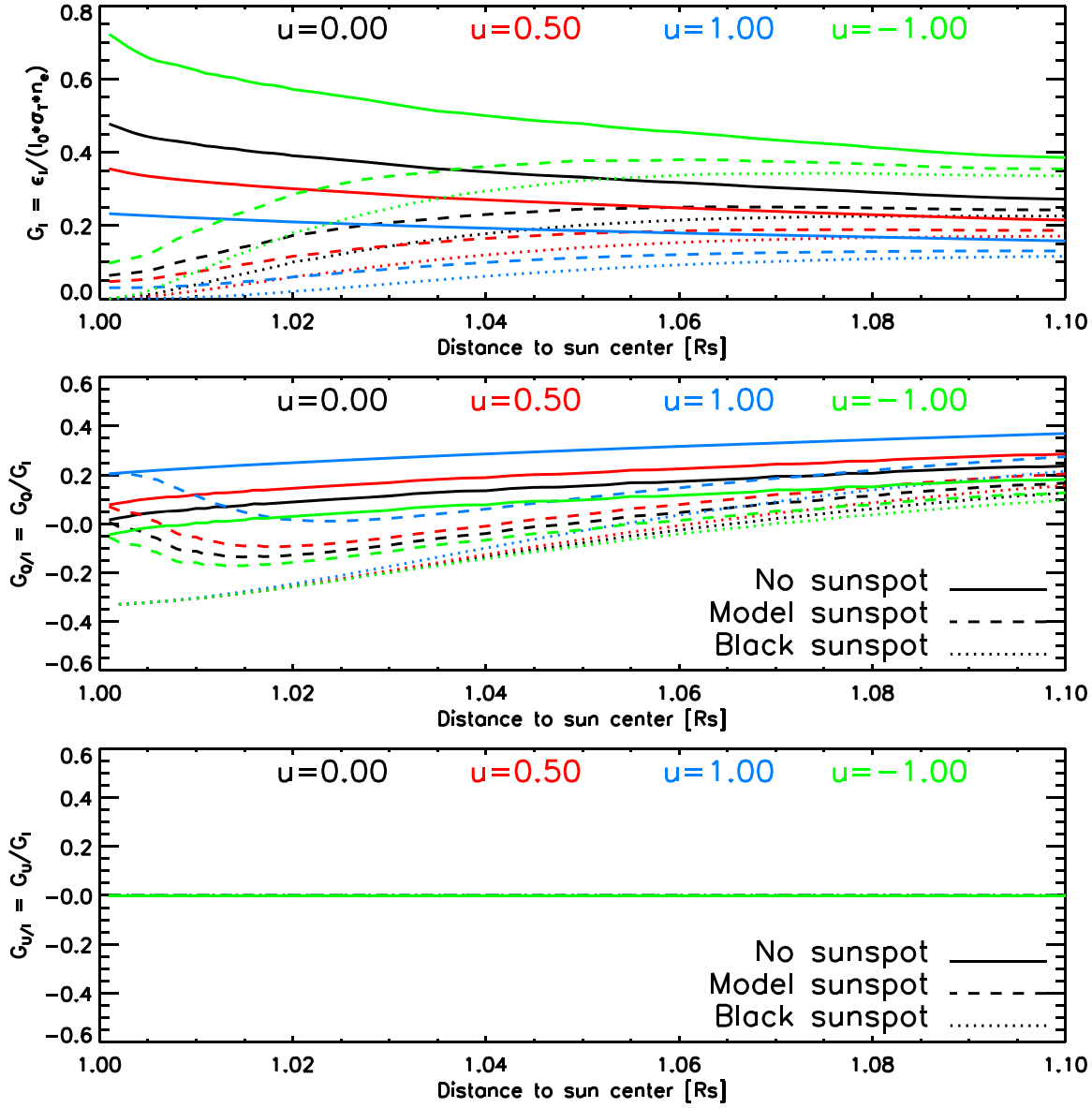

Figure 5. Stokes I emissivity and Q/I, U/I polarization for a scattering element of density n_e directly at the limb ($\chi = 90°$), and for various scatterer altitudes. The scatterer is directly on top of the sunspot.

In terms of perceived (by the observer) Stokes quantities, a base ($\boldsymbol{q}_p$, $\boldsymbol{q}_m$) must be defined by the observer. These unit vectors are perpendicular to the line of sight and each other. The component of the scattered electric fields oscillating along $\boldsymbol{q}_p$ contributes positively to Stokes Q, while the component of the scattered electric fields oscillating along $\boldsymbol{q}_m$ contributes negatively to Stokes Q (Figure 1). Similarly, a base ($\boldsymbol{u}_p$, $\boldsymbol{u}_m$) for Stokes U is defined, with $\boldsymbol{u}_p = (\boldsymbol{q}_p + \boldsymbol{q}_m)/\sqrt{2}$ and $\boldsymbol{u}_m = (\boldsymbol{q}_p - \boldsymbol{q}_m)/\sqrt{2}$. Note that the polarization base should ideally be defined with respect to the observer-to-scattering-element axis, and not e.g., the observer-to-Sun-center axis, though a fixed polarization base is what most instruments observe with. In this paper, we assume the latter configuration. The nuances are negligible in the cases considered here: for example, the deviation in ε_t goes as the square of the cosine of the Sun-center–observer–scatterer angle, or about 2×10^{-5} for a scattering element at the limb.

It follows that, at any one scatterer location, the following may be computed:

$$\eta_I = \eta_t + \eta_r, \tag{8}$$

$$\eta_Q = \eta_t\,(\boldsymbol{t}\cdot\boldsymbol{q}_p)^2 - \eta_r\,(\boldsymbol{r}\cdot\boldsymbol{q}_m)^2, \tag{9}$$

$$\eta_U = \eta_t\,(\boldsymbol{t}\cdot\boldsymbol{u}_p)^2 - \eta_r\,(\boldsymbol{r}\cdot\boldsymbol{u}_m)^2. \tag{10}$$

Integrating over the solar surface yields the emissivities of the scattering element

$$\varepsilon_i = \int \eta_i\, d\Omega_{\rm sun} = r_e^2\, n_e \int I_{\rm sun}\cdot g_i \cdot d\Omega_{\rm sun}, \tag{11}$$

where $i = I$, Q, or U. The integral covers the solar surface observable by the scattering element, with g_i a geometric factor map for each of the Stokes parameters (discussed in more detail in Appendix D). $I_{\rm Sun}$ can be replaced by $I_0\,p_{\rm Sun}$, where I_0 is the solar disk center intensity, and $p_{\rm Sun}$ a unitless

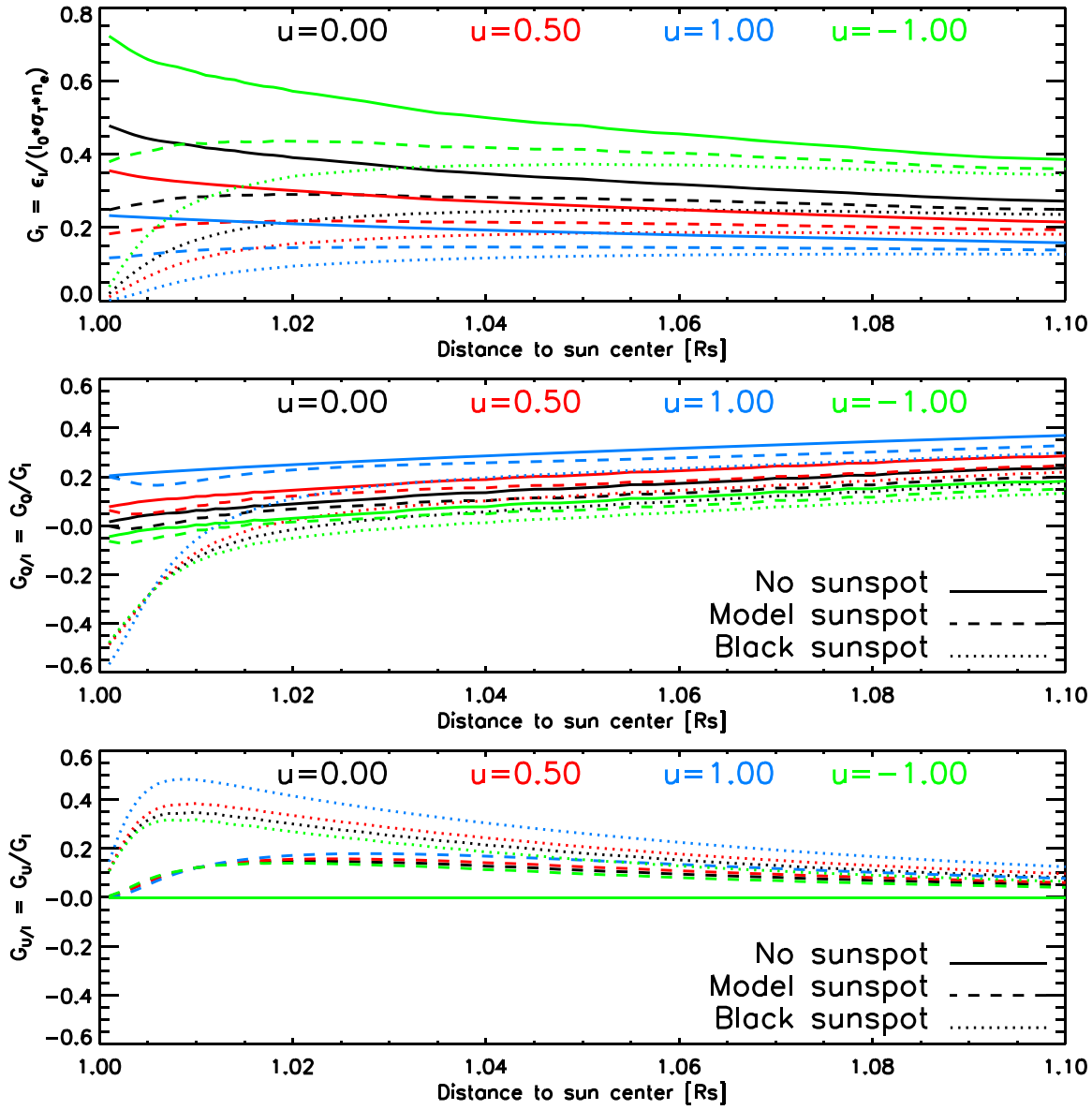

Figure 6. As with Figure 5, but with the sunspot centered 2.°7 north of the scatterer subpoint.

profile (Minnaert 1930 uses $p=\frac{I_{\rm SUN}}{I_0}=1\text{-}\upsilon+\upsilon\cos\Psi$, where Ψ is the scatterer–Sun-center–surface angle and υ is a limb-darkening coefficient) We then write

$$\varepsilon_i = r_e^2\, n_e\, I_0 \int p_{\rm sun}\cdot g_i \cdot d\Omega_{\rm sun} \tag{12}$$

$$= r_e^2\, n_e\, I_0\, G_i{}' \tag{13}$$

$$= \sigma_T\, n_e\, I_0\, G_i. \tag{14}$$

With the spatially integrated Thomson-scattering cross-section $\sigma_T = \frac{8\pi}{3} r_e^2$ ($=0.665\times10^{-28}$ m^2), the geometrical variations due to the limb-darkening profile and the presence of other features such as a sunspot are all included in the unitless factors G_i, in which the subscript i stands for Stokes I, Stokes Q, and Stokes U.

For the spotless Sun, G_I and G_Q are analytically given by Minnaert (1930) for various limb-darkening profiles. They depend only on altitude h and Minnaert's limb-darkening coefficient υ (see Appendix A). Note that because of symmetry, these cases have no Stokes U components ($G_U \equiv 0$).

In the cases where G_i does not vary too appreciably over the scatterer volume, an average can be used. The scattered intensity (as seen by the observer)[3] is determined by integrating over the line of sight:

$$I_i = \int \varepsilon_i\, d\ell, \tag{15}$$

$$\approx I_0\, \sigma_T\, <G_i> \int n_e\, d\ell \tag{16}$$

$$\approx I_0\, \sigma_T\, N_e\, <G_i>. \tag{17}$$

Integrating over the angular extent of the scattering material yields the scattered flux at the observer:

$$F_i = \int I_i\, d\Omega \tag{18}$$

[3] Note that the oft-used polarized brightness (pB) always has $\sqrt{Q^2+U^2}/I$ for amplitude, and is exactly equal to Q/I when Q > 0 is oriented tangential to the limb.

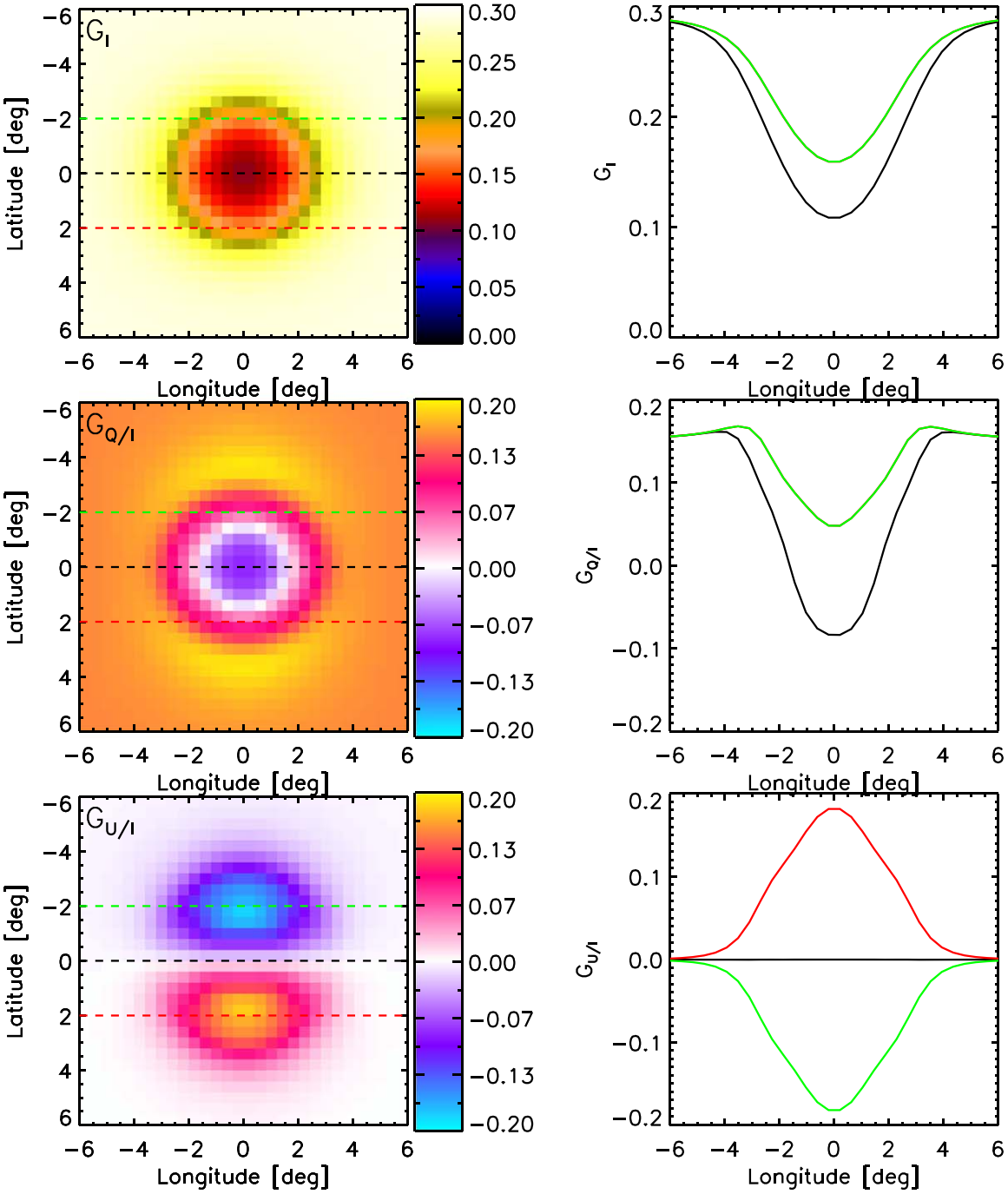

Figure 7. Left column: Stokes I flux, Q/I-, and U/I polarization v. the model sunspot location (lon/lat=(0,0) signifies that the sunspot is directly below the scatterer) $d = 1.02$, $\upsilon = 0.55$. Right column: some profiles corresponding to the dashed lines on the plots in the left column. Due to symmetry, the orange and red profiles sometimes overlap.

$$\approx I_0\, \sigma_T \; < G_i > \frac{1}{D^2} \int n_e \, dV \tag{19}$$

$$\approx I_0 \, \frac{\sigma_T}{D^2} \; < G_i > \; \mathcal{N}_e. \tag{20}$$

The subscript i stands for the Stokes parameters I, Q, or U: Stokes I $= F_I$, Stokes Q $= F_Q$, and Stokes U $= F_U$.

If the ratio I/I_0 can be determined from observations (e.g., simple pixel ratios), the free-electron column density N_e is hence simply extracted (at each pixel). Note that $\sigma_T N_e$ is furthermore a measure of the optical thickness (to Thomson scattering) of the line-of-sight column of scattering free electrons (and was found to be of order $\sim 10^{-3}$ or less in the event studied by Saint-Hilaire et al. 2014).

Assuming the case of the uniform Sun (no sunspots, no limb darkening) yields a useful order-of-magnitude approximation for most wavelengths from ~millimeter waves to UV (depicted in Figure 3):

$$\frac{F_I}{F_{\rm sun,I}} \approx \frac{F_I}{\pi \left(\frac{R_{\rm sun}}{D}\right)^2 I_0} \tag{21}$$

$$\approx < G_I > \; \frac{\sigma_T}{\pi R_{\rm sun}^2} \, \mathcal{N}_e. \tag{22}$$

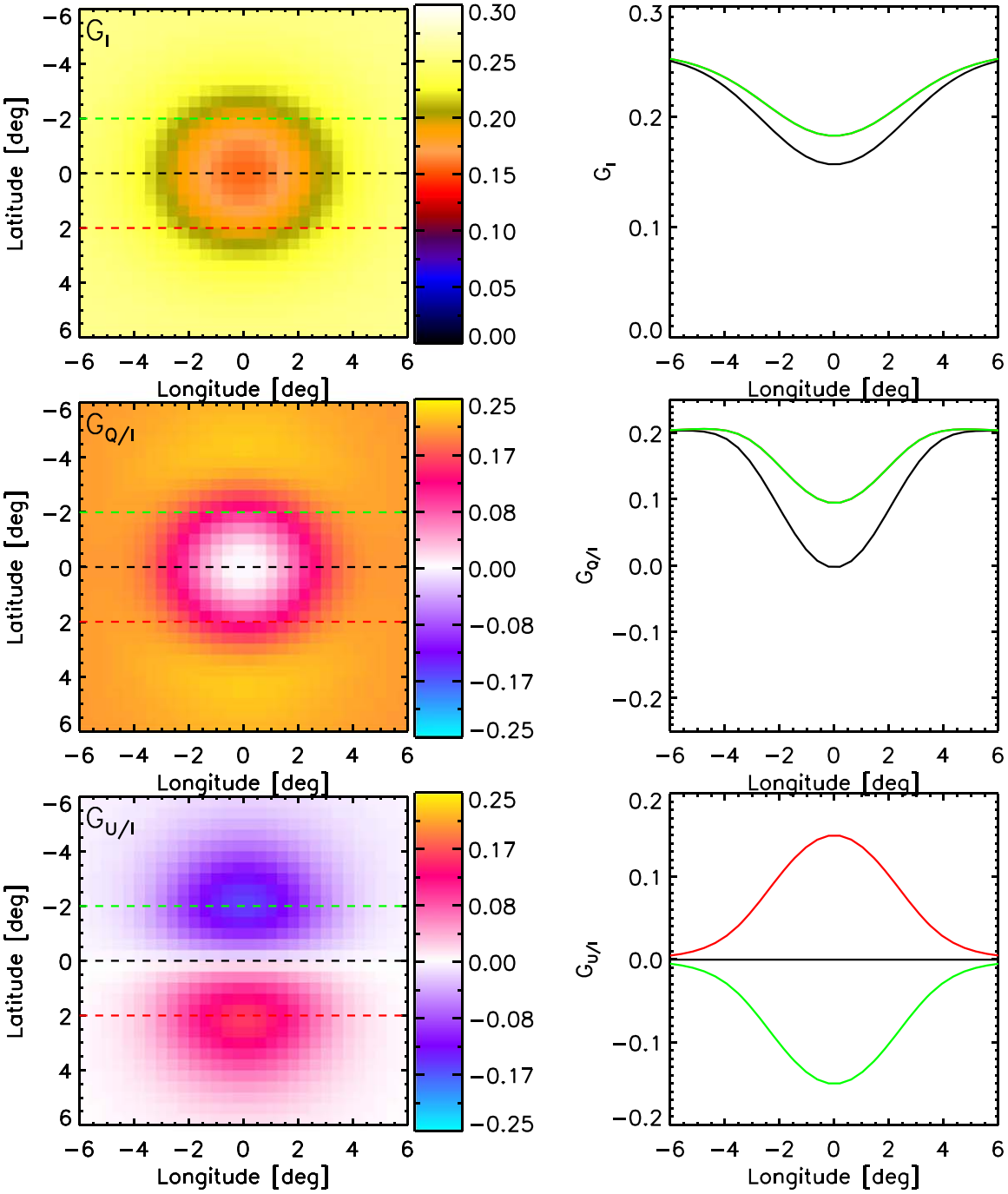

Figure 8. Same as Figure 7, but for $d = 1.04$.

That is, about 1.6×10^{-8} for $h = 0.04\ R_{\rm Sun}$, $\chi = 90°$, and $\mathcal{N} = 10^{39}$ electrons (and a mass of 1.7×10^{12} kg, assuming hydrogen-only plasma).

3. Numerical Integrations for an Axisymmetric Model Sunspot

We consider a model axisymmetric sunspot, with umbral and penumbral radii of 30″ and 51″ (as seen from Earth). These correspond to 0.031 $R_{\rm SUN}$ and 0.053 $R_{\rm SUN}$ in spherical distances on the solar surface (see Appendix B for angular correspondence from other viewpoints). The assumed umbral and penumbral intensities are, respectively, 0.13 I_0 and 0.5 I_0. Our model sunspot corresponds to an area of ≈ 1400 micro-solar hemispheres (msh), about half the area of the largest spot observed in the last three decades.

Figures 4(a)–(d) display solar intensity profiles and η_i-maps for various positions and limb-profile coefficients. The images show the sunspot as observed by the scatterer. The observer (at Earth) is to the far left, from the reader's (and scatterer's) perspective.

Figures 5 and 6 show the variations of the G_i factors with altitude, including, for reference, the case of a completely black sunspot ($I_{\rm SUN} \equiv 0$ within the spot).

Figures 7 and 8 display the G_i for various heliographic positions of our model sunspot with respect to the scatterer subpoint on the

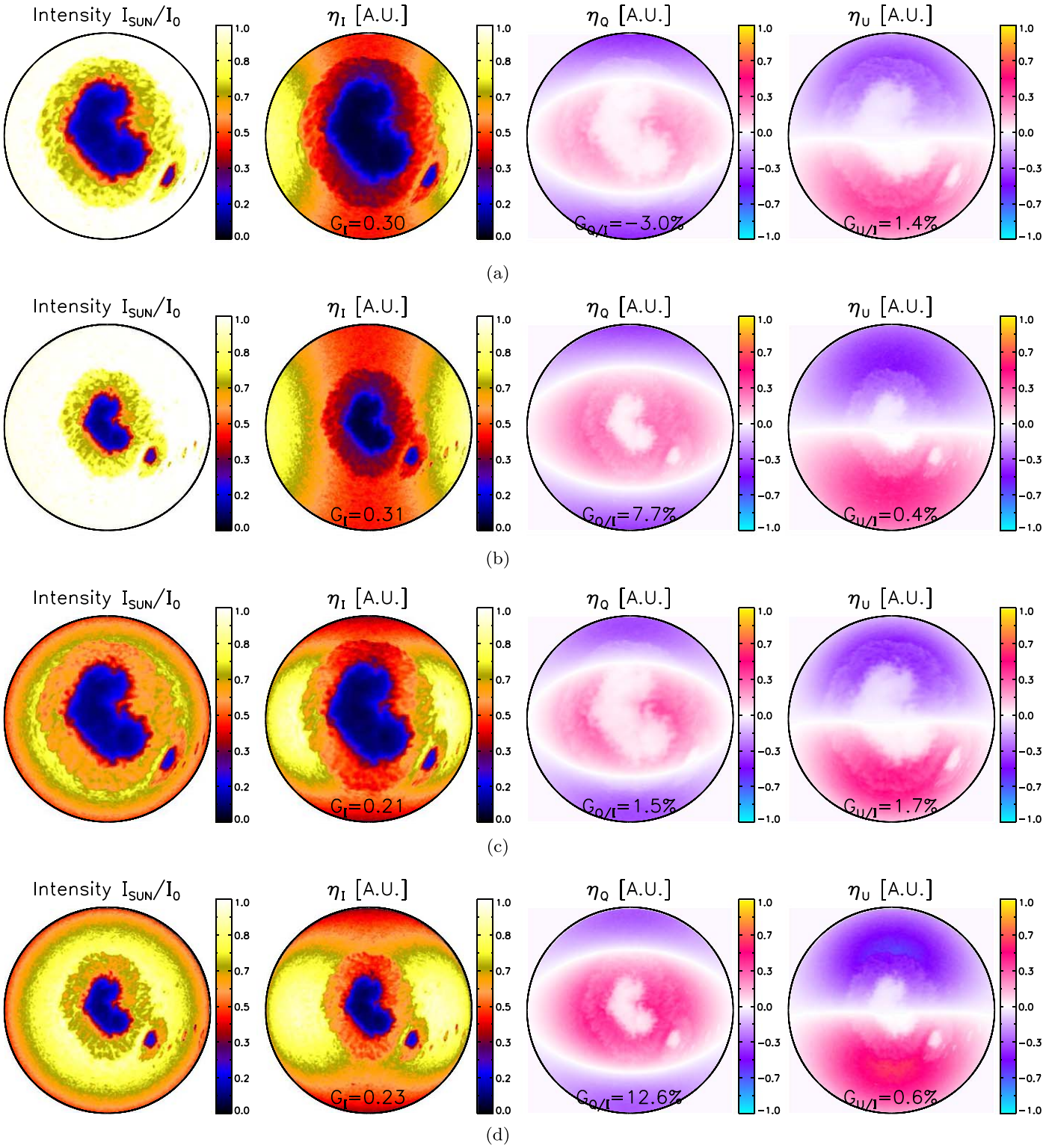

Figure 9. (a) Real sunspot #1: $d = 1.02$, $\upsilon = 0$; (b) real sunspot #1: $d = 1.02$, $\upsilon = 0.55$; (c) real sunspot #1: $d = 1.04$, $\upsilon = 0$; and (d) real sunspot #1: $d = 1.04$, $\upsilon = 0.55$.

solar surface, along with some profiles. Some observations, for the low altitudes ($d = 1.02$ and $d = 1.04$, or physical heights of 14 and 28 Mm) are:

1. If the scatterer subpoint is more than $\sim 6^\circ$ (about a penumbral diameter) or so away from the sunspot center, it has little effect.
2. Within that region, Stokes Q/I can be severally reduced (by up to tens of percents), or even become negative, and Stokes U/I can be close to as high in amplitude as the spotless Stokes Q/I (going either way in sign).

For low scatterer altitudes, it is clear that the sunspot location, with respect to the scatterer subpoint on the solar surface, can

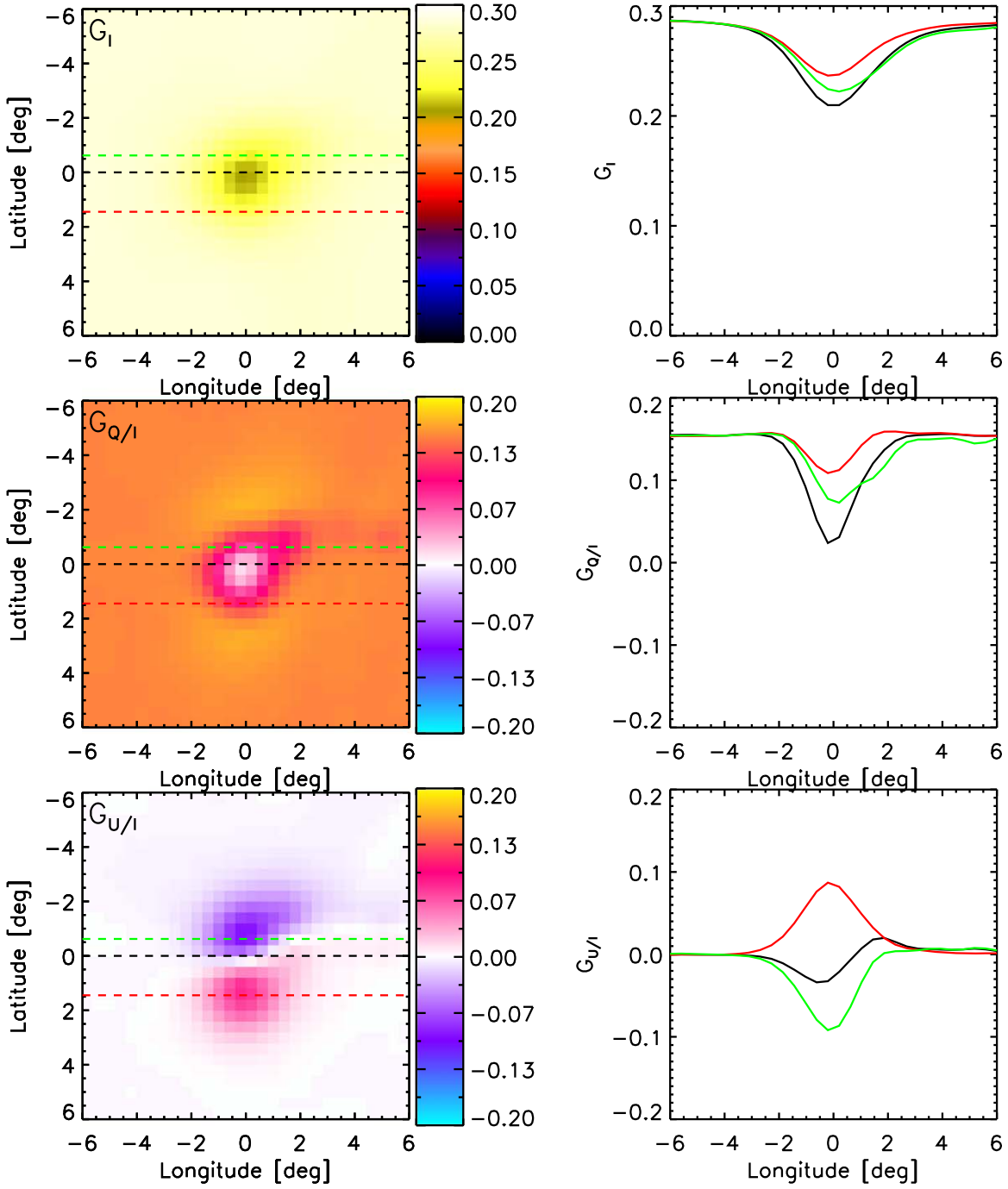

Figure 10. $d = 1.02$, $\upsilon = 0.55$.

have a drastic effect on Q/I and U/I. Though it is likely (though not automatic, as in cases of extreme symmetry) that when the effects are most severe, the presence of Stokes U/I polarization is strong.

4. Real Sunspots: Two Examples

We have also considered two detailed "real" sunspots, taken from SDO/HMI images around 2017 September 6 (a few days before the SOL2017-09-10 X8.2 flare). For both, we have removed the limb darkening (as perceived from 1 au), and replaced it with a limb-darkening profile (with a coefficient of $\upsilon \approx 0.55$) appropriate for the two altitudes considered. Any facular limb brightening (e.g., Labonte et al. 1984) has been neglected.

4.1. Real Sunspot #1

Figures 9, 10, and 11 pertain to National Oceanic and Atmospheric Administration (NOAA) Active Region #12674, taken on 2017 September 6 by SDO/HMI.

4.2. Real Sunspot #2

This sunspot (NOAA Active Region #12673, taken on 2017 September 6 by SDO/HMI) was in the other hemisphere as sunspot #1, and is the one which generated the SOL2017-09-10T15:35 X8.2 flare studied by Martínez Oliveros et al. (2022, in preparation) (Figures 12, 13, and 14).

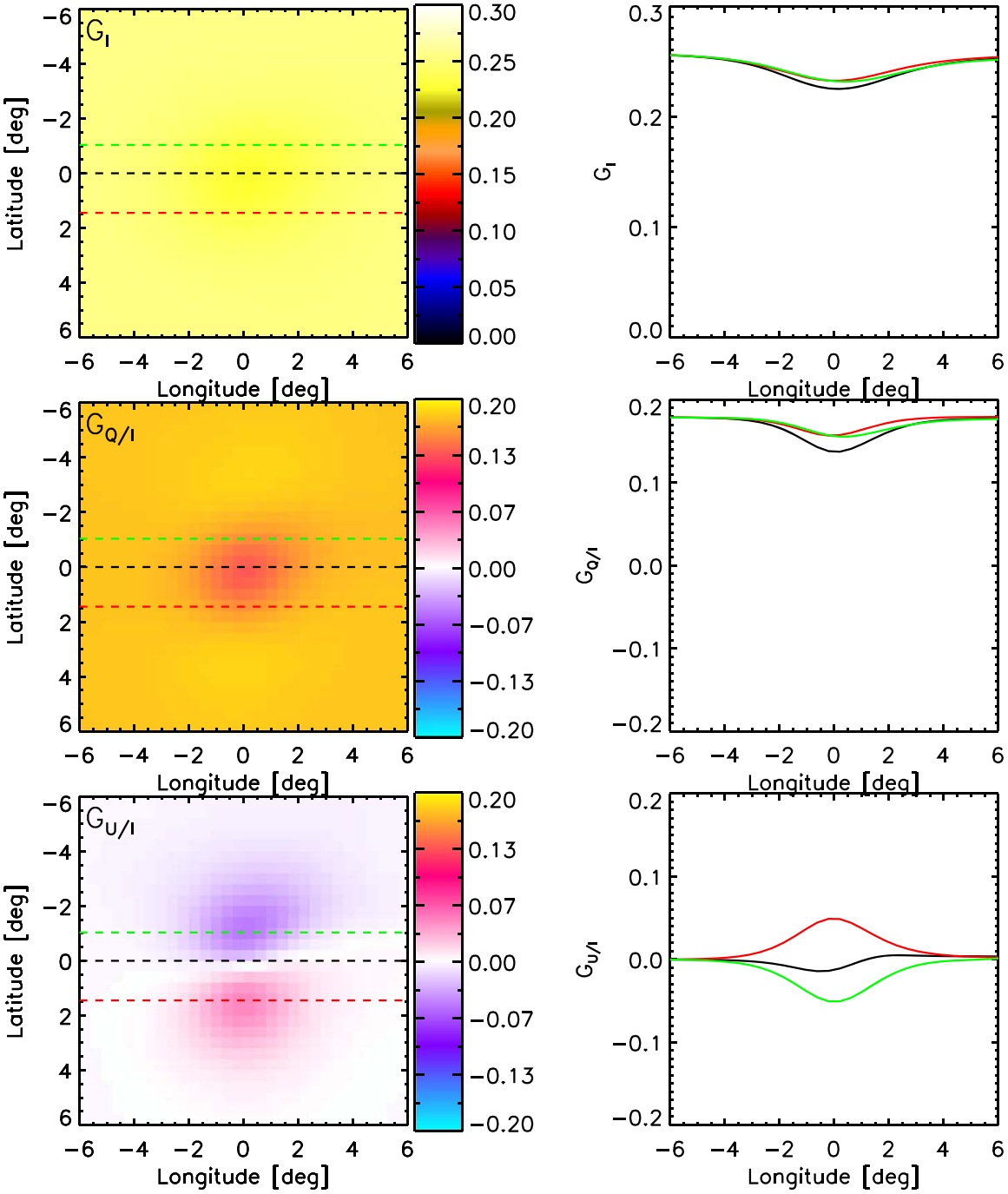

Figure 11. $d = 1.04$, $v = 0.55$.

4.3. Real Sunspots: Discussion

The results are qualitatively similar to what was found with our model sunspot, but with slightly smaller effects consistent with the areas. The effects at $d = 1.04$ are considerably less than those at $d = 1.02$, diminishing at vertical scales comparable to the sunspot's horizontal scales.

Assuming that the size and shape of AR 12673 were similar during the X8.2 flare, the effect of the sunspots at $d = 1.04$ is quite small: it is likely that any free-electron number determined assuming the no-sunspot case would be off by no more than a few tens of percents. At lower altitudes, the sunspot can have a much stronger effect, and is likely (except if roughly centered on the sunspot) to be detected through a strong Stokes U/I component.

5. Summary and Conclusion

This paper has numerically extended the classical (Minnaert 1930) treatment of continuum polarization in the low corona by assessing the effects of nonaxisymmetic radiation anisotropies due to sunspots. The numerical approach flexibly allows the use of any actual image of the photosphere; for best results this would require top views of an active region at the limb in order to be able to estimate the Stokes parameters via HMI or other observations of the low corona. We note that such top views

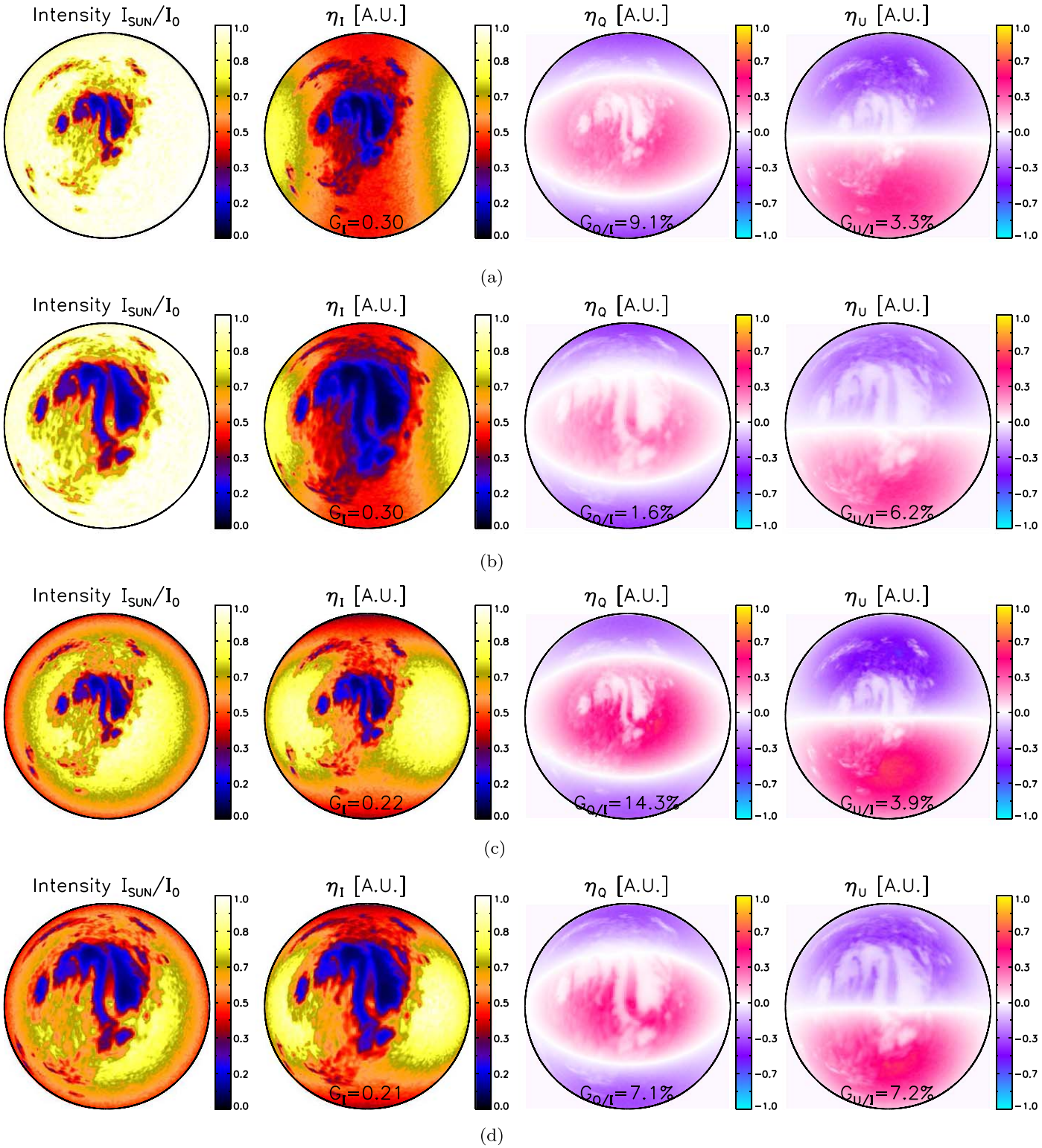

Figure 12. (a) Real sunspot #2: $d = 1.04$, $\upsilon = 0$; (b) real sunspot #2: $d = 1.02$, $\upsilon = 0$; (c) real sunspot #2: $d = 1.04$, $\upsilon = 0.55$; and (d) real sunspot #2: $d = 1.02$, $\upsilon = 0.55$.

should now be periodically available (at particular wavelengths) via Solar Orbiter (Solanki et al. 2020) observations. Our calculations follow Minnaert's in using a one-parameter limb-darkening function.

We find the following qualitative conclusions as well.

1. The effect of a sunspot is heavily dependent on how far away its center is from the scatterer subpoint. If it is more than about a diameter away, the effects are minimal and the Thomson-scattering problem is very close to the sunspotless case.

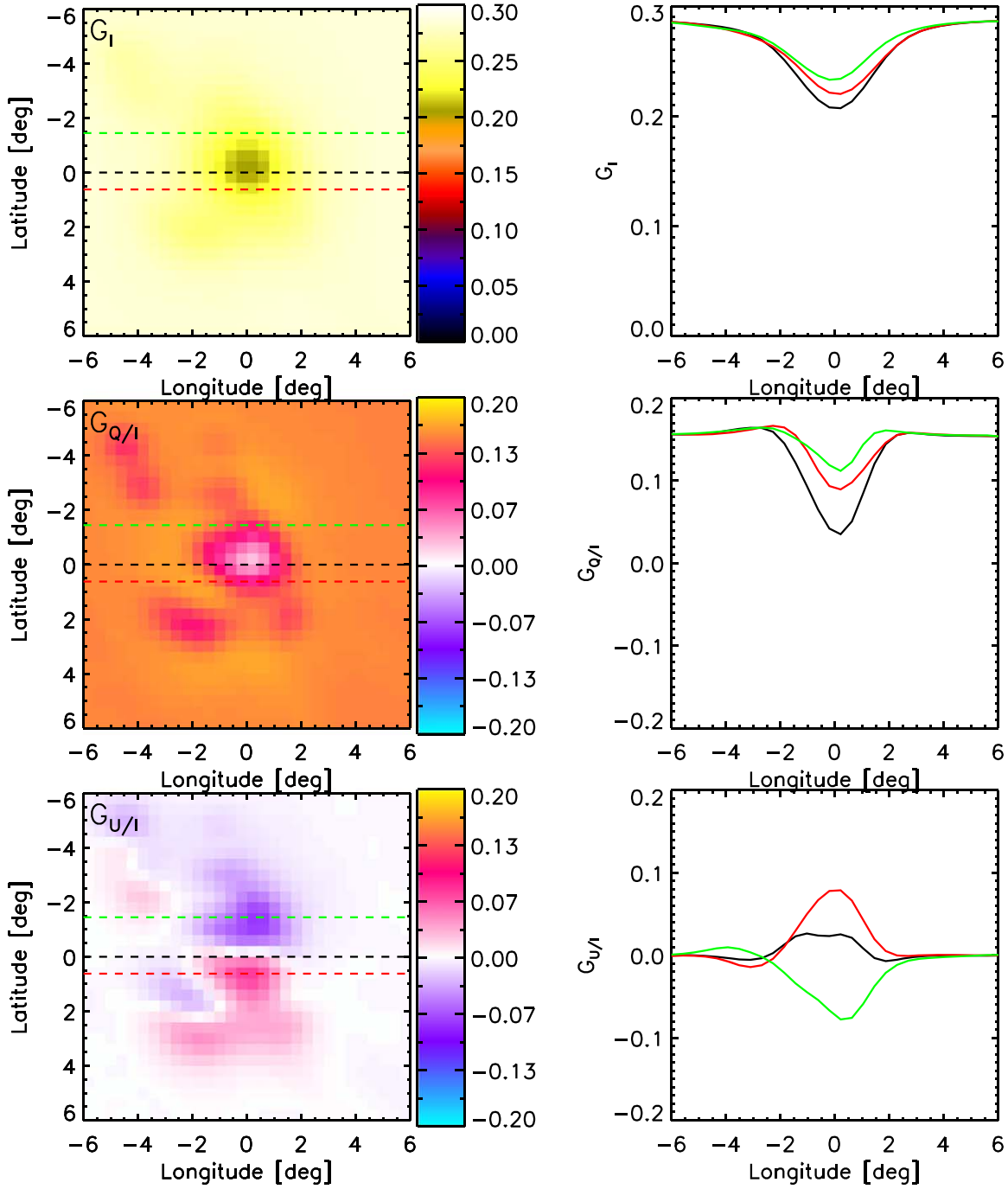

Figure 13. $d = 1.02$, $v = 0.55$.

2. The effect is also dependent on altitude. The higher the altitude, the closer we are to the sunspotless case, again on a height scale comparable to the spot's horizontal scale.
3. A sunspot can reduce Stokes I fluxes by several tens of percents or more.
4. A sunspot that significantly impacts free-electron (and mass) content calculations done assuming the spotless case is *likely* to show U/I polarization. However, in the unfortunate event that the scatterer subpoint is roughly centered on the sunspot, the U/I polarization can be small.

The effects of faculae remain to be incorporated into the modeling. Facular limb-darkening functions may not be well represented by a one-parameter model, and in any case are not well known just at the extreme limb (see papers in Labonte et al. 1984). This point is not trivial because observations of total solar irradiance have revealed strong shoulders of emission competing with sunspot dimmings (Willson et al. 1981). These time-series features presumably result from intense facular radiation at large vertical angles.

No U/I polarization is observed for the real sunspots corresponding to the two HMI flare events carefully studied to date (SOL2013-05-13T15:48 and SOL2017-09-10T15:35) and Q/I values above the hot loops are the theoretically expected ones for the spotless case. This leads us to conclude that the sunspots were either far from the scatterer subpoint on the solar surface, or perhaps fragmented to the point that they had little impact during the two flare events. The no-sunspot assumption

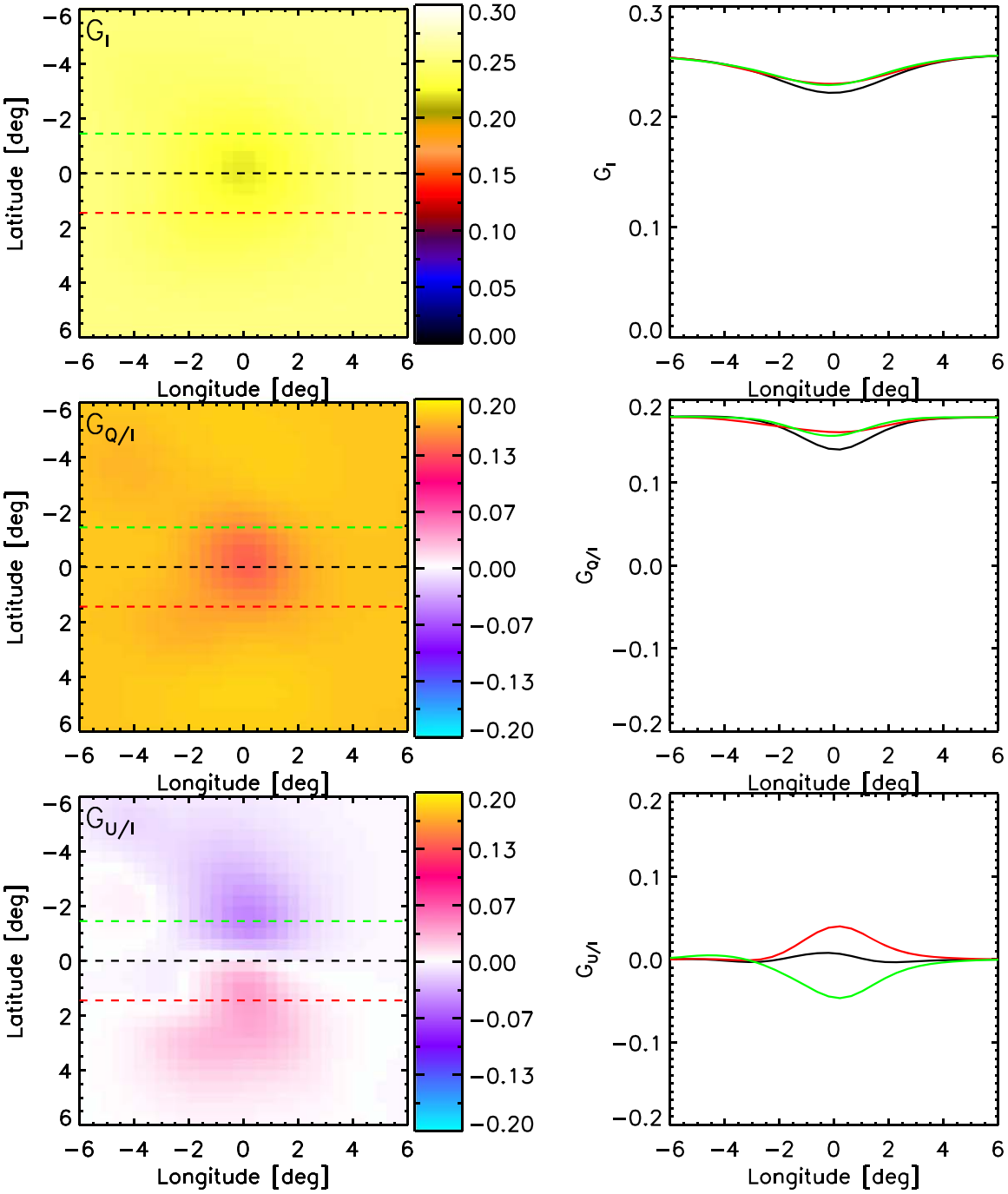

Figure 14. $d = 1.04$, $v = 0.55$.

used by Saint-Hilaire et al. (2014) and Martínez Oliveros et al. (2014) should hence yield reasonably accurate (within a few tens of percents) electron and mass content. Ideally, observations of the flaring sunspot off the observer–Sun line are needed to determine the sunspot shape at the flare time and the exact position of the scattering mass with respect to it. On-disk observations of the active region several days before/after the event may serve as good proxy for the former, but localization is better obtained with a stereoscopic approach.

This modeling activity, limited as it is to the case of single-parameter limb-darkening laws, should be immediately applicable to the many HMI above-the-limb flare events (and we plan on making our software available to the community). It also suggests that a combination of modeling and observation of active-region polarization, possibly taking advantage of imaging from Solar Orbiter, may help to clarify solar limb-darkening laws at the extreme limb, a matter of broad significance.

We thank Petr Heinzel, whose useful comments have helped improve this manuscript. This work was partially supported by NASA grant 80NSSC18K1257.

Appendix A
Thomson-scattered Intensity and Polarization for the Uniform Sun and No Limb Darkening/Brightening

$$\frac{1}{r_e^2 n_e}\frac{\varepsilon_t}{I_0} = \frac{\pi}{2}\left(\frac{4}{3} - \cos\Omega - \frac{\cos^3\Omega}{3}\right) \tag{A1}$$

$$\frac{1}{r_e^2 n_e}\frac{\varepsilon_r}{I_0} = \frac{\pi}{2}\left(\frac{4}{3} - \cos\Omega - \frac{\cos^3\Omega}{3} - \cos\Omega\sin^2\Omega\sin^2\chi\right) \tag{A2}$$

Here, $\Omega = \arcsin\frac{1}{d}$ is the angle from the Sun-center–scatterer line to the scatterer's horizon on the solar surface. Minnaert (1930) presents the full analytical solutions for the limb-darkening profile $I = I_0(1 - \upsilon + \upsilon\cos\Psi)$, with υ being a limb-darkening coefficient ($\upsilon = 0$ means uniform Sun; $\upsilon \approx 0.55$ is the appropriate coefficient for 6173 Å). The angle Ψ is the scatterer–Sun-center–surface angle (see Figure 1 of Minnaert 1930).

Here, t and r are defined with respect to the Sun center, not with respect to any solar surface element, as done in the main manuscript.

From those, the intensity and degree of linear polarization can be derived as

$$\frac{1}{r_e^2 n_e}\frac{\varepsilon_t + \varepsilon_r}{I_0} = \pi\left(\frac{4}{3} - \cos\Omega - \frac{\cos^3\Omega}{3} - \frac{1}{2}\cos\Omega\sin^2\Omega\sin^2\chi\right) \tag{A3}$$

$$\frac{\varepsilon_t - \varepsilon_r}{\varepsilon_t + \varepsilon_r} = \frac{\cos\Omega\sin^2\Omega\sin^2\chi}{2\left(\frac{4}{3} - \cos\Omega - \frac{\cos^3\Omega}{3}\right) - \cos\Omega\sin^2\Omega\sin^2\chi} \tag{A4}$$

$$= \frac{1}{2\frac{\frac{4}{3} - \cos\Omega - \frac{1}{3}\cos^3\Omega}{\cos\Omega\sin^2\Omega\sin^2\chi} - 1} \tag{A5}$$

$$= \frac{G_Q}{G_I} = G_{Q/I} \tag{A6}$$

$$= \frac{\text{Stokes Q}}{\text{Stokes I}}. \tag{A7}$$

Here, because of symmetry, Stokes $U = 0$ and $G_U = 0$, and the same holds for nonuniform (but symmetric) limb profiles. The presence of sunspots and an active region can break the symmetry, leading to non-zero Stokes U.

Replacing r_e^2 with $\sigma_T = \frac{8\pi}{3}r_e^2$ in Equation (A3), it becomes

$$\frac{1}{\sigma_T n_e}\frac{\varepsilon_t + \varepsilon_r}{I_0} = \frac{1}{2}\left(1 - \frac{3}{4}\cos\Omega - \frac{\cos^3\Omega}{4} - \frac{3}{8}\cos\Omega\sin^2\Omega\sin^2\chi\right) \tag{A8}$$

$$= G_I, \tag{A9}$$

where $G_I(d, \upsilon)$ is a geometrical factor Stokes I function computed for a featureless Sun but with limb-darkening coefficient υ, determined analytically from, e.g., the work of Minnaert 1930. $G_I(d, \upsilon = 0)$ is simply the case with no limb darkening/brightening, i.e., uniform surface brightness.

Figure 15 displays G_I and $G_{Q/I} = G_Q/G_I$ for various υ.

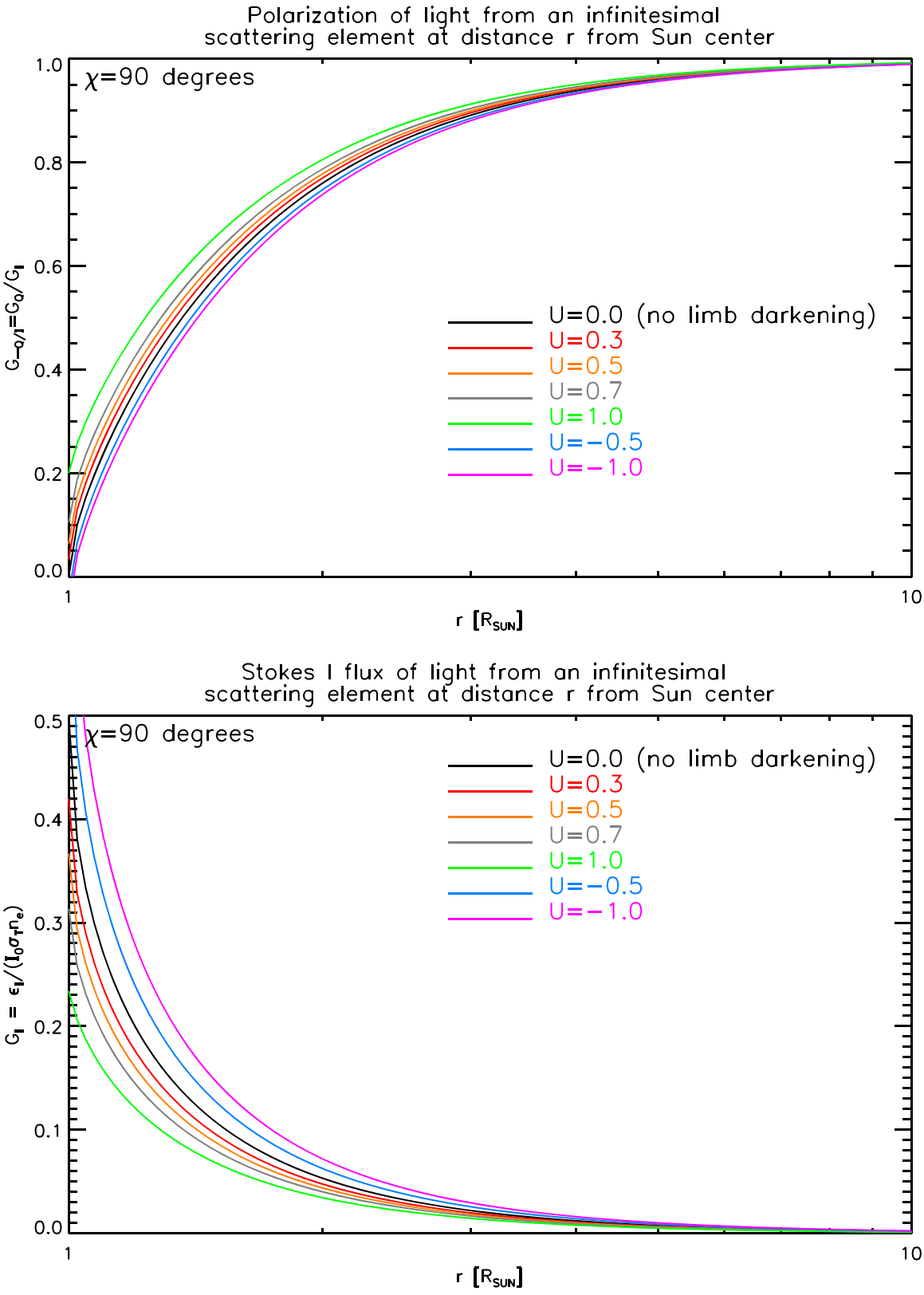

Figure 15. Q/I polarization levels and Stokes I fluxes for various limb-darkening coefficients υ (Minnaert 1930). For reference, $\upsilon = 0$ corresponds to a uniform Sun (∼extreme infrared), and $\upsilon = 0.55$, 0.6, and 0.8 to the solar limb-darkening profiles at 617.3 nm, 570 nm, and 430 nm. The profiles for $\upsilon < 0$ are also shown. They can be construed as limb-brightening profiles without any above-the-limb component (such as the typical factor two jump).

Appendix B
Various Angles of Interest

Figures 16 and 17 display scatterer horizon, sunspot umbral and penumbral angular sizes as perceived from Earth, Sun center, or the scatterer.

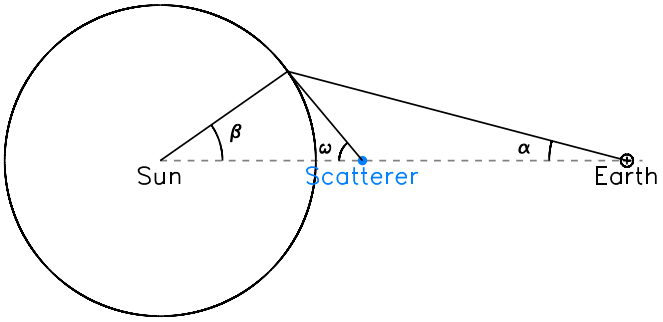

Figure 16. Geometry for the angles displayed in Figure 17. The Sun center, scatterer, and Earth (observer) have been here aligned for simplicity.

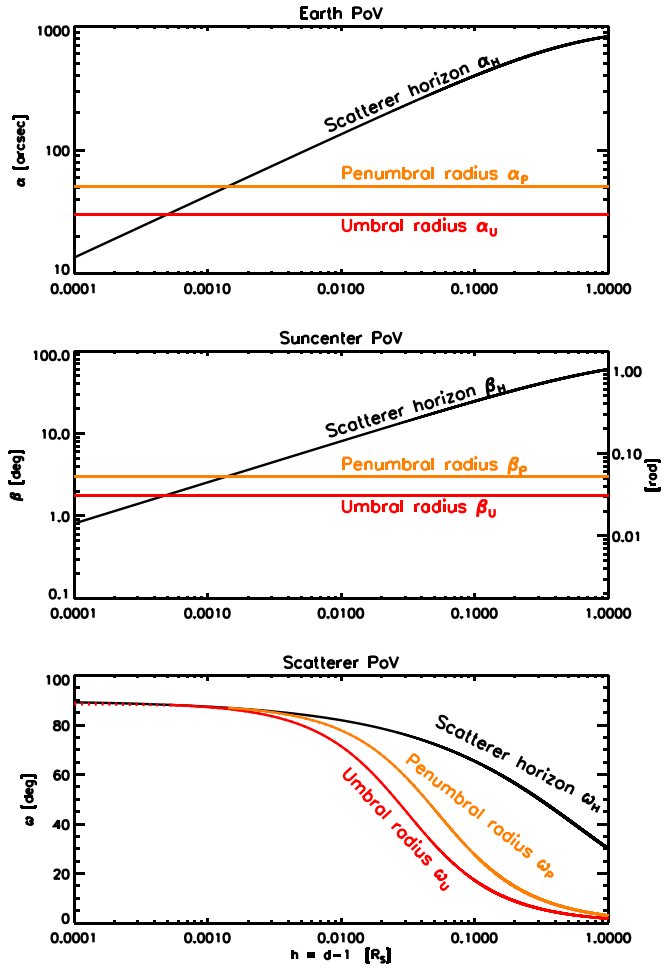

Figure 17. Model sunspot angular extent from various viewpoints (see, e.g., Figure 16). At altitudes $h \lesssim 0.0013\ R_S$, the scatterer is so low that its horizon is filled by the sunspot, and at altitudes $h \lesssim 0.0005\ R_S$, the umbra fills the whole horizon on the solar surface.

Appendix C
Filling Factors

Filling factor η defined such that the density of emitting electrons is

$$n_e = \frac{\mathcal{N}}{\eta V} \tag{C1}$$

with V being the observed volume, and ηV being the emitting volume. $\mathcal{N}$ is the total number of free electrons in volume V. With such a definition, the volume emission measurement is

$$EM = n_e^2\ \eta V = \frac{\mathcal{N}^2}{\eta V}. \tag{C2}$$

Hence, computing the total number of electrons from the observables EM, V, $\mathcal{N} = \sqrt{EM \cdot \eta V}$, or the total kinetic energy in thermal electrons, $E_{\rm th}{=}\frac{3}{2}k_B T\sqrt{EM \cdot \eta V}$, depend on the knowledge of η (it is often assumed to be unity).

Diagnostics linearly dependent with density, such as Thomson scattering, do not suffer from this problem, and are hence of great value. Combining with the above, η can be determined. (Note that spectral line ratios can also yield n_e.)

Appendix D
Geometrical Factor Maps g_i

The g_i geometrical factor maps from Equation (11) only depend on three parameters: the distance to the Sun center d (which also sets the field of view to the solar surface); χ_0, the scattering angle at map center, and ρ, the rotation angle between the local radial (as seen by the observer) and the observer's Q < 0 reference:

$$g_i = \frac{1}{r_e^2 n_e}\frac{\eta_i}{I_{\rm SUN}}\ [sr^{-1}]\ ,\ i = I,\ Q,\ U. \tag{D1}$$

Hence, all the η_i maps can be computed by multiplying the $I_{\rm SUN}$ map (the leftmost map in the row of Figures 4, 9, and 12) by $r_e^2 n_e g_i$.

Figure 18 displays a set of those universal g_i maps for two altitudes ($d = 1.02$ and $d = 1.04$), scattering angle $\chi_0 = 90°$, and $\rho = 0°$ (i.e., the $Q > 0$ axis is tangential to the limb, and the $Q < 0$ axis is the radial direction projected on the plane of the sky (both from the observer's perspective)).

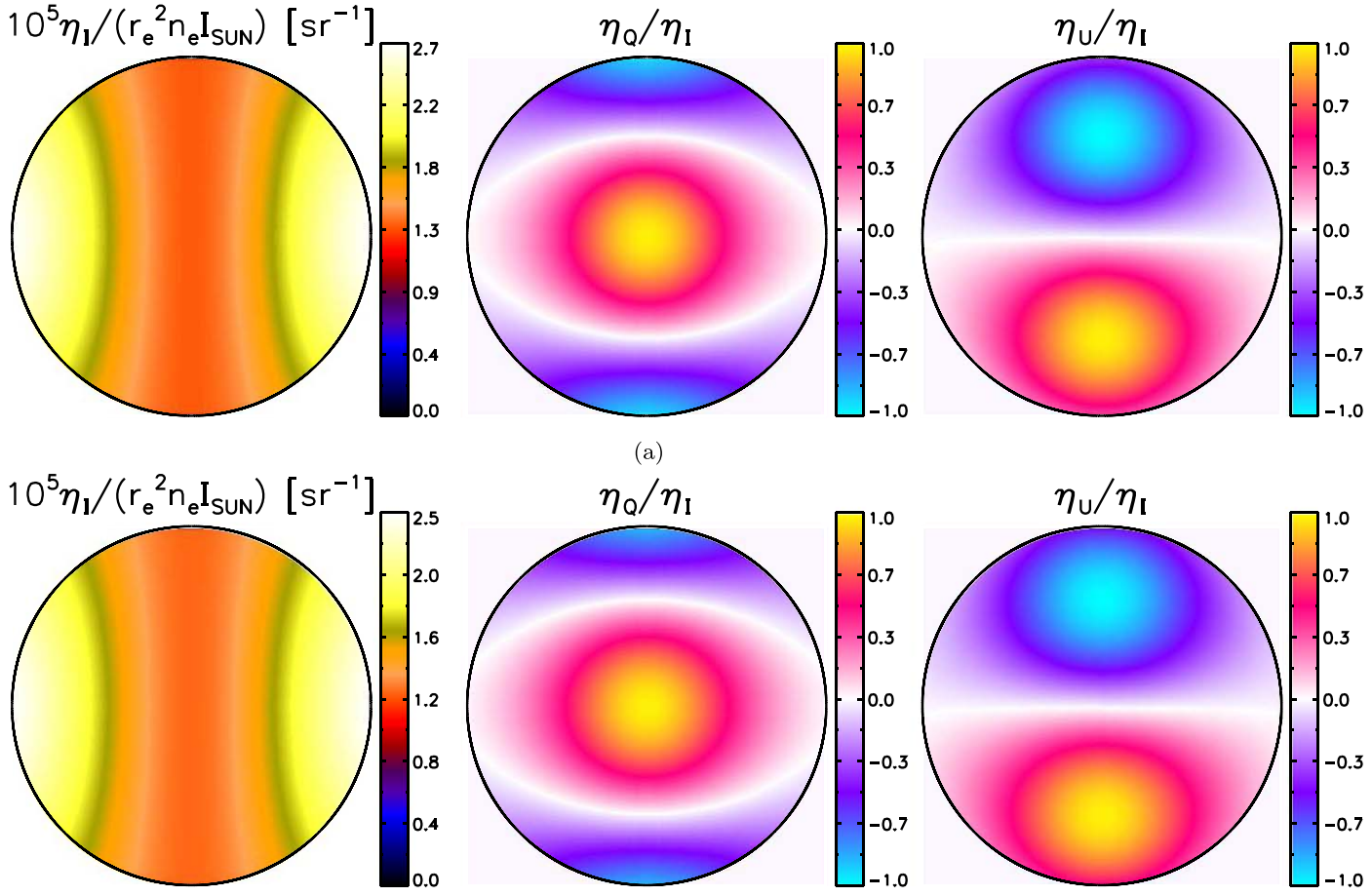

Figure 18. Geometrical factor maps g_I, g_Q/g_I, and g_U/g_I. (a) $d = 1.02$, $\chi_0 = 90°$; (b) $d = 1.04$, $\chi_0 = 90°$.

ORCID iDs

Pascal Saint-Hilaire https://orcid.org/0000-0002-8283-4556
Hugh S. Hudson https://orcid.org/0000-0001-5685-1283

References

Derouich, B. M. 2018, PASP, 130, 034203
Jackson, J. D. 1975, Classical Electrodynamics (New York: Wiley)
Jejčič, S., & Heinzel, P. 2009, SoPh, 254, 89
Jejčič, S., Kleint, L., Heinzel, P., et al. 2018, ApJ, 867, 134
Labonte, B. J., Chapman, G. A., Hudson, H. S., et al. 1984, Solar irradiance variations on active region time scales, NASA Conf. Publ., NASA CP-2310 (Washington, DC: NASA)
Martínez Oliveros, J.-C., Krucker, S., Hudson, H. S., et al. 2014, ApJL, 780, L28
Minnaert, M. 1930, ZAp, 1, 209
Pesnell, W. D., Thompson, B. J., & Chamberlin, P. C. 2012, SoPh, 275, 3
Saint-Hilaire, P., Schou, J., Martínez Oliveros, J.-C., et al. 2014, ApJL, 786, L19
Scherrer, P. H., Schou, J., Bush, R. I., et al. 2012, SoPh, 275, 207
Schou, J., Scherrer, P. H., Bush, R. I., et al. 2012, SoPh, 275, 229
Solanki, S. K., del Toro Iniesta, J. C., Woch, J., et al. 2020, A&A, 642, A11
Willson, R. C., Gulkis, S., Janssen, M., Hudson, H. S., & Chapman, G. A. 1981, Sci, 211, 700